



Contents lists available at ScienceDirect

Earth and Planetary Science Letters

www.elsevier.com/locate/epsl



Prolonged ascent and episodic venting of discrete magma batches at the onset of the Huckleberry Ridge supereruption, Yellowstone

Madison L. Myers^{a,*}, Paul J. Wallace^a, Colin J.N. Wilson^b, Beth K. Morter^a,
Elliot J. Swallow^b

^a Department of Geological Sciences, University of Oregon, Eugene, OR 97403-1272, USA

^b School of Geography, Environment and Earth Sciences, Victoria University, PO Box 600, Wellington 6140, New Zealand

ARTICLE INFO

Article history:

Received 19 December 2015
Received in revised form 12 July 2016
Accepted 12 July 2016
Available online xxxx
Editor: T.A. Mather

Keywords:

Huckleberry Ridge Tuff
explosive eruption
fall deposits
melt inclusions
volatile concentrations
diffusive losses

ABSTRACT

How exceedingly large, volcanic supereruptions begin provides crucial information on the storage, ascent and release of silica-rich magma in catastrophic events. Initial fall deposits of the 2.08 Ma, 2500 km³ Huckleberry Ridge eruption are multiply bedded and in several places contain reworked intervals, indicating time breaks in the opening phases of the eruption. A 2.5 m section of these fall deposits was sampled at nine levels below the earliest ignimbrite (member A) at Mount Everts (Mammoth, Wyoming). We analyzed major and trace elements and volatiles in quartz-hosted melt inclusions (MIs), reentrants (REs; unsealed melt inclusions) and associated obsidian pyroclasts (thick-walled shards) to establish quartz crystallization and storage depths and melt compositional groupings. Systematic relationships between Rb and other incompatible elements (U, Cl, B) indicate ~55% fractional crystallization between the least and most evolved glass compositions. In contrast, H₂O concentrations in MIs show scattered relationships with trace elements and are interpreted to reflect variable loss of H₂O by diffusion through the quartz host during magma ascent. The wide H₂O variations (1.0–4.7 wt.%) in MIs from individual fall horizons imply as much as ~14 days of diffusive loss, reflecting highly variable and surprisingly slow decompression conditions. Water and CO₂ gradients in reentrants, however, are consistent with final ascent times of <1 to 4 h (ascent rates of ~0.3–1.5 m/s), similar to those represented by MIs that we infer to have experienced little to no diffusive H₂O loss. The wide range of ascent rates for co-erupted crystals mirrors that of intermittent explosive activity at Mount St. Helens in summer 1980, and implies that the Huckleberry Ridge magma body was not strongly overpressured at eruption onset. Restored entrapment pressures and geochemical data for MIs provide evidence for six distinct populations of quartz that originally crystallized in geochemically distinct magma domains. The compositions of REs and obsidian pyroclasts, by comparison, show that by the onset of eruption, the quartz had been brought together into three discrete magma bodies, which we interpret to have been cupolas on the roof of the main magma body. These cupolas were erupted sequentially and episodically from separate vents to generate the fall deposits before escalating activity led to generation of voluminous pyroclastic flows, and this pattern of activity suggests that tectonic triggering may have destabilized multiple magma bodies. Supereruptions as large as the Huckleberry Ridge event may start hesitatingly if the parental magma bodies are not strongly overpressured, with small-scale episodic activity that is modulated by external controls that may leave no other geological evidence for their presence.

© 2016 Elsevier B.V. All rights reserved.

1. Introduction

Caldera-forming silicic eruptions are among the most devastating natural events on Earth, with the largest (supereruptions) disgorging vast quantities of material on geologically instantaneous timescales (Mason et al., 2004; Self, 2006). However, the mechanisms and timescales associated with eruption onset remain un-

clear. Do such eruptions start vigorously, then escalate (Wilson and Hildreth, 1997), or can there be episodicity (Wilson, 2001), and what might cause an explosive eruption to stop once initiated? Although most researchers agree that overpressure due to magma recharge or volatile exsolution is a common triggering mechanism in small-volume chambers (Roche and Druitt, 2001; Jellinek and DePaolo, 2003; Gregg et al., 2012), there remains controversy about its role in larger, caldera-forming eruptions (see Gregg et al., 2015). In the latter case, there is also debate as to

* Corresponding author.

E-mail address: mmyers3@uoregon.edu (M.L. Myers).

<http://dx.doi.org/10.1016/j.epsl.2016.07.023>

0012-821X/© 2016 Elsevier B.V. All rights reserved.

whether buoyancy is central to the initiation (Caricchi et al., 2014; Malfait et al., 2014) or if an external mechanism, such as roof destabilization or tectonic rifting, is a requirement for mobilization (Gregg et al., 2012, 2015; de Silva and Gregg, 2014). This controversy is exacerbated by a scarcity of geochemical data on the very earliest deposits from supereruptions that could constrain how they start. However, discriminating between these mechanisms is possible (e.g. Allan et al., 2012) if the state and behavior of magma at eruption onset could be assessed. In particular, because magma ascent rates reflect the extent of overpressure in the magma chamber (e.g., Melnik and Sparks, 1999), determining ascent rates for the earliest erupted materials can reveal whether or not internal triggering by overpressure in the source magma body was important.

Here we address these issues by combining field evidence with evaluation of magma ascent timescales derived from diffusive H₂O losses from enclosed melt inclusions (MIs) and H₂O and CO₂ loss from reentrants (REs; unsealed melt inclusions), all preserved in quartz phenocrysts. We take advantage of the inferences that significant diffusive loss of H₂O species from MIs through their host phenocryst can occur on timescales of hours to days during magma rise (Severs et al., 2007), and from REs on even shorter timescales associated with the final stages of magma ascent (Liu et al., 2007; Humphreys et al., 2008; Lloyd et al., 2014). We couple our timescale information with micro-scale geochemistry to examine magma chamber conditions and conduit processes shortly before and during the opening stages of the Huckleberry Ridge supereruption.

2. Geological background

The Huckleberry Ridge Tuff (HRT) is the product of the oldest and largest (2.08 Ma; 2500 km³) of the three caldera-forming eruptions at the Yellowstone Plateau volcanic field (Christiansen, 2001; Fig. 1). The HRT consists of initial fall deposits overlain by three voluminous welded ignimbrite units [members A, B and C], with minor additional fall deposits beneath member C. Here we focus on the initial fall deposits beneath member A, which consist of multiple bedded layers, including several that are normally graded up to fine ash tops. This grading implies that the eruption plume stopped and restarted several times, reflecting episodicity during the opening explosive phases. In addition, there is evidence in these deposits for reworking in their lower parts at multiple stratigraphic levels, observed in widely-spaced stratigraphic sections (Fig. 1b, c and Supplementary Fig. 1). A lack of wholesale reworking or significant gullying of the fine-grained ash-rich beds, however, precludes time periods of months to years for any single hiatus, but rather requires pauses in deposition on the order of days (see also Supplementary Fig. 1).

3. Methods

Nine individual layers were sampled from the lowest 1.8 meters of the 2.5 m thick, largely unconsolidated fall deposits preserved beneath the welded base of ignimbrite member A on the western rim of Mt. Everts near Mammoth, Wyoming, north of the inferred eruptive source (Fig. 1a). The nine sampled layers were chosen to bracket horizons of reworking and to be distributed over changes in grain size (Fig. 1b). At higher levels than those sampled, the fall deposits are baked or fused by the overlying welded ignimbrite, the matrix glasses are darkened and MIs devitrified; this material was not used in this study. Samples were sieved to 500 μm and picked for loose, but glass-coated, quartz crystals. Individual crystals were mounted and doubly polished to expose glassy, bubble-free MIs and REs (Fig. 2). Size, glass color, and distance from the

nearest crystal rim were recorded for each MI (Online Supplementary Table 1) and cathodoluminescence images of the quartz hosts were acquired (Supplementary Fig. 2). We report data only from those samples with pristine and glassy MIs, which are thus inferred to have quenched rapidly on eruption, preserving information about their entrapment and ascent histories. Black obsidian shards to micro-pyroclasts (<1 mm across) from each layer were also sampled, and mounts prepared and analyzed in a similar manner to the MIs and REs.

Water and CO₂ concentrations were measured using a Thermo Nicolet Nexus 670 Fourier transform infrared (FTIR) spectrometer interfaced with a Continuum IR microscope at the University of Oregon. Absorbances measured were converted to H₂O and CO₂ concentrations using the Beer–Lambert law ($c_i = M_i \cdot A / \rho \cdot d \cdot \varepsilon$), where c_i is the concentration of the absorbing species, M_i is the molecular weight of the species (g/mol), A is the absorbance (height) of the relevant vibration band, ρ is the glass density (g/L), d is the thickness of the wafer analyzed (cm) and ε is the molar absorption coefficient (L/mol cm). In rhyolitic compositions, ρ and ε strongly depend on total H₂O concentration. This requires the use of an iterative process to converge on appropriate values [Eq. (1) Skirius, 1990 and Eq. (2) Leschik et al., 2004]:

$$\rho = 2350 - 12.6 C_{\text{H}_2\text{O}} \quad (1)$$

$$\varepsilon = 80 - 1.36 C_{\text{H}_2\text{O}} \quad (2)$$

where $C_{\text{H}_2\text{O}}$ is the concentration of total dissolved H₂O in wt.%. Final densities using Eq. (1) range from 2295–2336 kg/m³, and final ε values using Eq. (2) are between 73 and 79 L/mol cm. Total H₂O concentration was calculated using the 3570 cm⁻¹ peak, which required that thicknesses for the quartz wafers be between 30 and 70 μm. For thicker wafers, total H₂O was calculated using the near IR peaks (5230 cm⁻¹ and 4520 cm⁻¹; Zhang et al., 1997). The absorption coefficient (ε) for molecular CO₂ (2350 cm⁻¹) in rhyolitic glass is 1214 L/mol cm (Behrens et al., 2004). Peak heights were calculated using a straight-line background correction (Dixon et al., 1995). Thicknesses were measured using both a digital micrometer (±2 μm) and the reflectance interference fringe method (Wysoczanski and Tani, 2006). Agreement between the two methods is within 4 μm.

After FTIR analysis, the quartz and obsidian pyroclast wafers were set in a 1-inch epoxy mount for analysis of major elements using a Cameca SX-100 electron microprobe (EPMA) at University of Oregon. Operating conditions were 15 kV and 10 nA sample current for Si, Ca, Na, Fe, Al, and K, and 50 nA current for Cl, F, Mg and Ti. A beam size of 5–10 μm was used for all analyses. Sodium, K, Si, and Al were measured first, and their concentrations were calculated using a time-dependent intensity correction in Probe for Windows (Donovan et al., 2007). Glasses were then analyzed for trace elements by Laser-Ablation Inductively Coupled Plasma Mass Spectrometry (LA-ICP-MS) at Oregon State University using a 50 μm spot size, with five glass standards (GSD-1G, BHVO, ANTO, NIST-612, and BCR) for calibration, ²⁹Si as an internal standard, and GSD-1G as a check standard throughout the run. Major, trace, and volatile element concentrations, along with their associated errors, can be found in Online Supplementary Table 1 (MIs and REs) and Online Supplementary Table 2 (obsidian pyroclasts).

4. Results

All quartz-hosted MIs and REs from the nine stratigraphic levels sampled are high silica rhyolite (SiO₂ = 75–77 wt.%, volatile-free). The data show a negative correlation between SiO₂ and Al₂O₃, consistent with compositional control dominated by feldspar crystallization (Fig. 3a). Concentrations of U (6–10 ppm), Cl (1200–2000 ppm), and B (9–20 ppm) produce continuous arrays

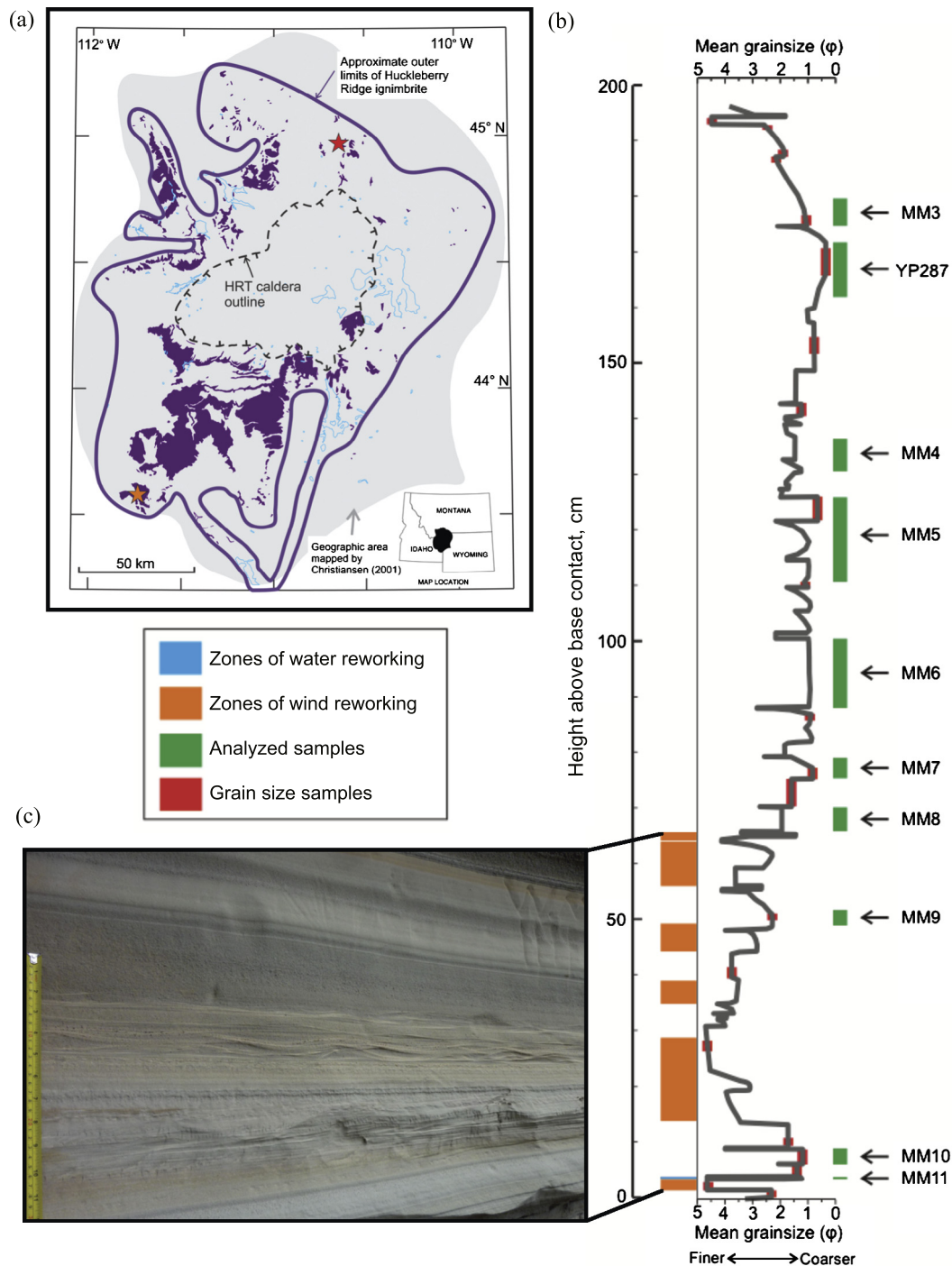


Fig. 1. (a) Outline map of the area covered by ignimbrite of the Huckleberry Ridge Tuff. The geographical area mapped by Christiansen (2001) is shown by gray shading, purple areas represent outcrops of the ignimbrite, and the purple line represents its approximate outer limits. The red star denotes the location at Mt. Everts of the fall deposit section (panel b), which shows evidence of reworking (panel c). The orange star marks a locality in Swan Valley, 180 km SSW of Mount Everts, where correlated reworking horizons have been identified (see Supplementary information). (b) Stratigraphic representation of the lower part of the 2.5 meter-thick HRT initial fall deposits on Mt. Everts. Green zones represent samples reported on here. The red fields indicate samples that were collected for sieve analysis and used to calibrate the grain size variation curve shown. Zones of reworking (see Supplementary Fig. 1) are also shown as colored fields: zones of water reworking (one blue sliver affecting the layer sampled as MM11), and zones of wind reworking (in orange). (c) View of the lower, fine-ash-dominated portion of the HRT fall deposits at Mount Everts. Note the two prominent zones of inferred wind reworking within the fine ash deposits, and the sharp break (horizon 'h': see Supplementary Fig. 1, Panel G for detail) into the coarser ash to fine lapilli middle parts of the fall deposits (at ~65 cm above base in the stratigraphic log). (For interpretation of the references to color in this figure legend and in all subsequent figures, the reader is referred to the web version of this article.)

when plotted against Rb (170–270 ppm), which is expected to be incompatible during crystallization (Fig. 3b, e). Using appropriate partition coefficients and an equilibrium crystallization model (see Fig. 3 caption) the range of compositions is consistent with ~55% crystallization of the least-evolved MI compositions in the middle and upper sampled layers to yield the most-evolved MI composi-

tions in the earliest layers sampled. Some trace elements (e.g. Ba, Sr), however, tend to cluster the MI data into distinct groups rather than produce continuous arrays (e.g. Fig. 3f). Although REs and obsidian pyroclasts largely overlap in composition with the MIs from their equivalent layer (Supplementary Fig. 3), they are more closely clustered than the MIs (see discussion in Section 6).

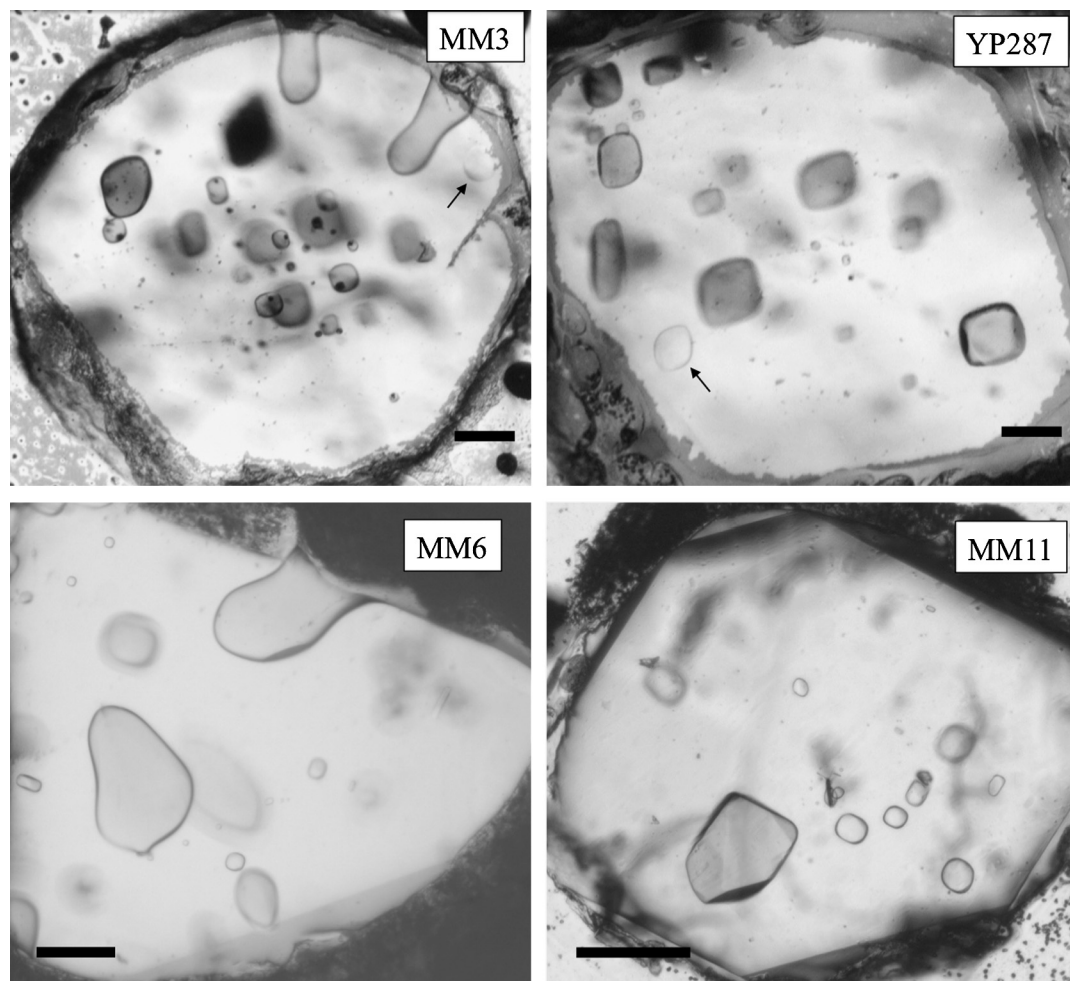


Fig. 2. Photomicrographs of quartz-hosted MIs and REs typical of samples from the fall section. Samples MM3 and YP287 contain both colorless and brown MIs; arrows point to colorless MIs. A 100 μm scale bar is shown in each image.

In each fall horizon sampled, including the lowermost (<2–3 cm above the basal contact, likely the first $\leq 0.1 \text{ km}^3$ of erupted magma), there is a wide range of H_2O contents (~ 1.0 to 4.5 wt.%) in sealed MIs (Fig. 4, Supplementary Fig. 4b). This is in contrast to the factor of two variation preserved by other incompatible elements (e.g. Rb: Fig. 3, Supplementary Fig. 4a). Although the majority of inclusions analyzed are colorless, higher up in the fall deposit samples YP287 and MM3 contain both colorless and brown inclusions, sometimes in the same crystal. The colorless inclusions in MM3 and YP287 contain much lower H_2O and higher CO_2 concentrations than the brown inclusions, and overall are smaller in volume and/or closer to the crystal edge. In all other sampled horizons, the lowest- H_2O MIs are in grains that do not contain high- H_2O MIs. Additionally, cathodoluminescence (CL) images of the quartz hosts show no evidence that any of the lower- H_2O MIs were trapped by late-stage growth of crystal rims (cf. Peppard et al., 2001; Supplementary Fig. 2).

5. Causes of volatile variations and modeling of magma ascent timescales

5.1. H_2O concentrations from quartz-hosted MIs

The wide range of H_2O values in MIs from each sampled layer compared to the more limited variation in Rb concentration is best explained by diffusive loss of H species through the quartz host crystal during ascent (Severs et al., 2007). Consistent with this

interpretation, Li, which also has a relatively rapid diffusivity in quartz (Charlier et al., 2012), is also highly scattered when plotted against Rb (Fig. 3c). This scatter contrasts strongly with the consistency shown by all other major and trace elements, which diffuse through quartz at much slower rates. Thus we interpret the MIs with the highest H_2O values to reflect magmatic concentrations at the storage depth prior to eruption, and the lower values to reflect variable diffusive losses, suggesting that at a given stratigraphic horizon, co-deposited crystals experienced different ascent histories and decompression rates (Supplementary Fig. 4b). The variable H_2O concentrations can be used to calculate a decompression timescale for each MI and host crystal if initial and external melt concentrations of H_2O can be constrained. However, timescales cannot be estimated using the Li variations because of complexity in Li solubility and diffusivity (Charlier et al., 2012).

Alternative explanations for the wide range of MI H_2O values in co-deposited quartz crystals include reheating of the fall deposit by the thick overlying ignimbrite, and recycling (after ~ 1 day to a week) of crystals from hot, surficial deposits. If reheating by overlying ignimbrite was important, the crystals in any layer would have all experienced the same temperature–time history. As a result, there would be a more uniform distribution of H_2O values within a given layer (with H_2O values more strongly correlating with inclusion volume, e.g. Lloyd et al., 2013), and there should be systematic trends through the section (i.e., more diffusive loss at the top, in closer proximity to ignimbrite). None of these features are observed. Recycling of quartz from hot, near-vent sur-

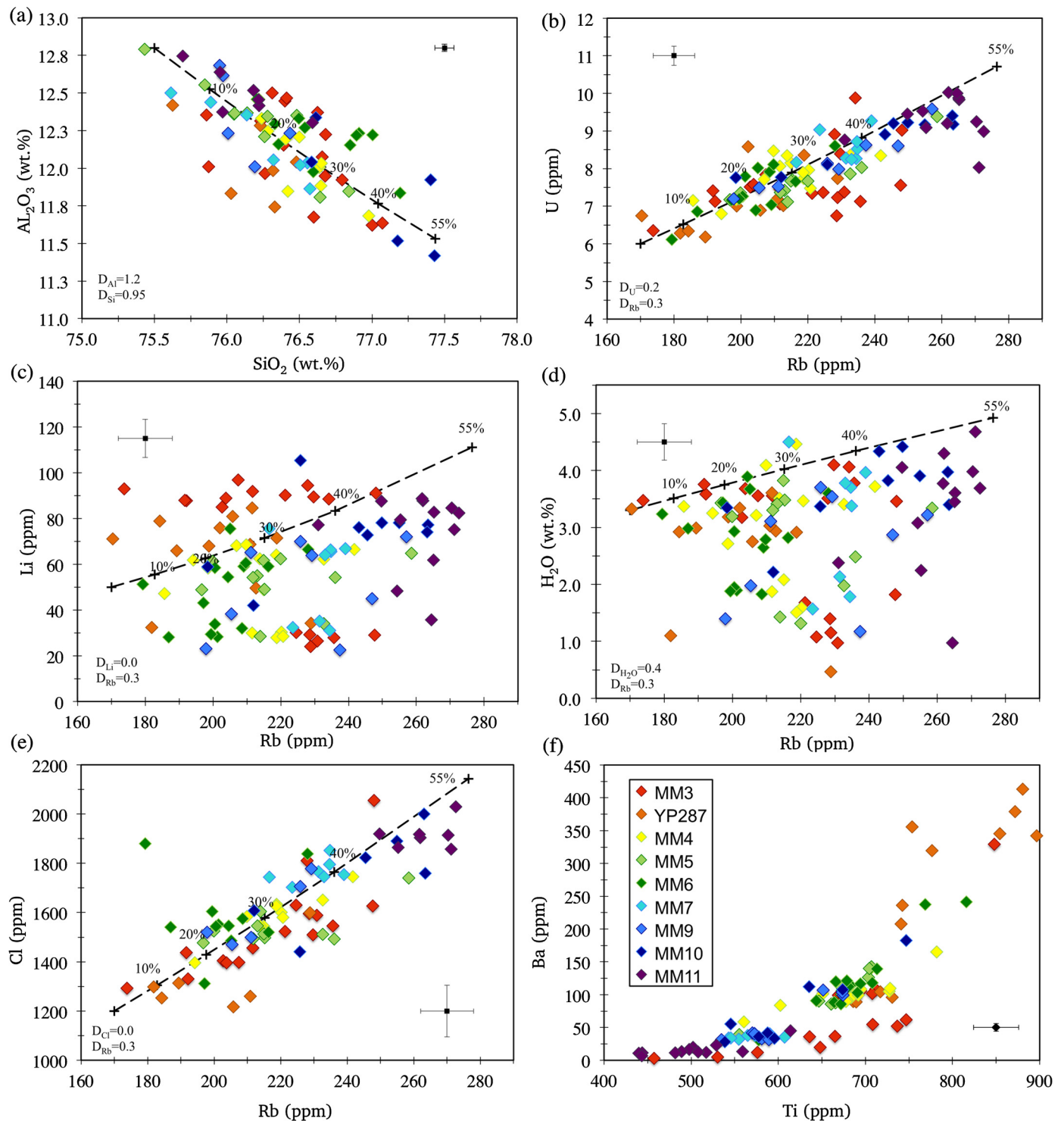


Fig. 3. Volatiles and trace elements vs. Rb for MIs from the nine layers sampled from the HRT fall deposit (see Fig. 1). Legend is shown in lower right panel. Curves show equilibrium crystallization (in wt.%) calculated using bulk partition coefficients as follows: $D = 0$ for Cl and Li, $D = 0.3$ for Rb, and $D = 0.2$ for U (Roberge et al., 2013), appropriate for a high-silica rhyolite crystallizing quartz and two feldspars, with biotite and amphibole absent. For H_2O , $D = 0.4$ was used to simulate crystallization of vapor-saturated rhyolitic melt (see discussion in text). Error bars show average 1 SE analytical uncertainties. Uncertainties for individual MI analyses can be found in Online Supplementary Table 1.

ficial deposits could create the variable H_2O values, but there is no evidence for dome-derived material (obsidian pyroclasts contain detectable concentrations of CO_2) or for thermal oxidation of, or microlite growth in, the selvage glasses. In addition, none of the inclusions are devitrified, nor are there fragments of recycled tuff found as lithic material. Based on these observations, we interpret the range of H_2O values in MI in co-deposited crystals to

be the result of highly variable ascent histories and decompression rates of magma within the conduit system.

5.2. Temperature estimates

To calculate timescales associated with diffusive losses of H_2O through the quartz hosts, we need to constrain the pre-eruptive

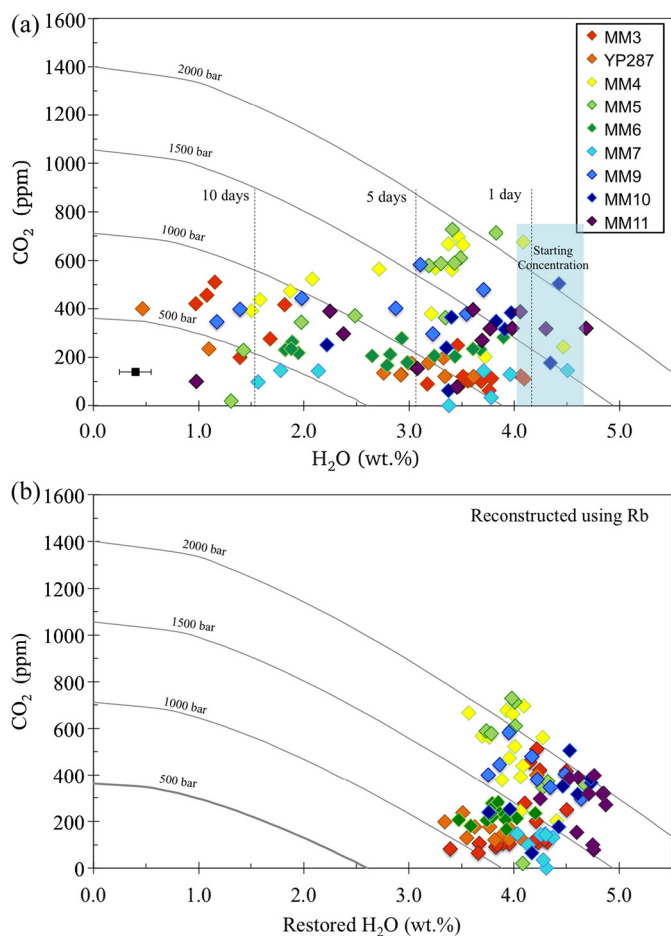


Fig. 4. (a) H₂O vs. CO₂ for MIs from the HRT fall deposit. Curves show vapor saturation isobars calculated at 800 °C using VolatileCalc (Newman and Lowenstern, 2002). Error bar in lower left of top panel shows mean SE analytical uncertainties, where SE for CO₂ is less than symbol size. (b) Restored H₂O values, calculated as described in the text, vs. CO₂ for all MIs.

temperature of the HRT fall deposit magma because diffusivity of H-species in minerals is strongly temperature dependent (e.g., Johnson and Rossman, 2013). Experimental phase equilibria on compositionally similar rhyolites from the Bruneau–Jarbridge eruptive center of the Yellowstone hotspot track have been determined at pressures of 2 and 5 kbar, with H₂O concentrations up to 4 wt.% (Almeev et al., 2012). In the more applicable 2 kbar experiments (see Fig. 4), the mineral assemblage present in the HRT A fall deposit (quartz, plagioclase, sanidine) occurs in equilibrium with melt containing 4 wt.% H₂O at 800 °C. Glass compositions from the experiments at these conditions are similar to our average MI composition (Online Supplementary Table 3), with the largest discrepancy found in Na₂O (Almeev et al., 2012: 2.85 wt.%; HRT MI: 3.78 wt.%). In agreement with the Almeev et al. (2012) experimental phase equilibria and H₂O concentrations from MIs, application of the plagioclase–melt hygrometer of Waters and Lange (2015) using plagioclase and matrix glass compositions from our samples (E.J.S., unpublished data) yield melt H₂O concentrations of 4.0–4.5 wt.% at 800 °C.

For comparison, we also calculated zircon saturation temperatures. Using the Watson and Harrison (1983) calibration, the average temperature for all MI and RE is 800 ± 24 °C (2σ; see Online Supplementary Table 1 for calculated temperatures). The Boehnke et al. (2013) calibration, however, yields lower values of 753 ± 28 °C. The magnitude of the offset between the two methods in these compositions was noted by Boehnke et al. (2013). Given the agreement between the phase equilibrium, plagioclase–

melt hygrometer results, and Watson and Harrison (1983) temperatures, and the observation that the Boehnke et al. (2013) calibration gives temperatures that are consistently lower than other geothermometers in rhyolitic systems (e.g. Barker et al., 2014; Loewen and Bindeman, 2015), we use 800 °C as the pre-eruption magmatic temperature. However, because of the implications surrounding the temperature estimate, the diffusion calculations presented in the next section were also calculated at 775 and 825 °C for samples from a single horizon (Supplementary Fig. 5). We find that the uncertainty in our temperature estimate has a minor effect on our calculated timescales (factor of ±1.6) and does not affect our overall conclusions.

5.3. Ascent timescales based on diffusive H loss from MIs

Calculating a timescale of diffusive H loss from each MI through the quartz host requires an estimate of (1) the diffusion coefficient of H in quartz, (2) the H₂O partition coefficient between quartz and melt (0.001: Qin, 1992), (3) the initial MI H₂O concentration, and (4) the external H₂O concentration. We calculate a diffusion coefficient of 10⁻¹¹ m²/s using the diffusion model of Cottrell et al. (2002) and the experimental data of Severs et al. (2007) on H diffusive losses from MI in quartz at 800 °C.

To approximate the initial H₂O contents (before diffusive loss) we applied two methods. In the first, we assumed that H₂O behaved moderately incompatibly through partial loss to a vapor phase during vapor-saturated crystallization (Roberge et al., 2013; Fig. 3). During crystallization, the fact that H₂O is much more soluble than CO₂ causes dissolved H₂O to increase in the melt, but to a lesser extent than it would if the system was not vapor saturated. A vapor–melt partition coefficient of 0.4 can explain the variations observed for least-degassed melt inclusions from all samples (Fig. 3d), and represents a similar value to model results for vapor-saturated crystallization using rhyolite-MELTS with included H₂O and CO₂ solubility relations (Ghiorso and Gualda, 2015). Using the calculated fractionation curve in Fig. 3d, we estimate the initial (restored) H₂O content of each MI based on its composition (Fig. 4b).

The second method is based on an assumption that the MIs were trapped with variable Rb and H₂O and then held in a magma chamber such that all MIs re-equilibrated to the surrounding H₂O concentration, regardless of their variable Rb (Fig. 3, Supplementary Fig. 3a). In such a scenario, the highest H₂O concentration of MIs from each sample would best estimate the initial H₂O concentration at that stratigraphic level. This method yields starting values of 3.7–4.5 wt.% H₂O (Fig. 4a, Supplementary Fig. 4b), whereas the first method using Rb gives 3.3–4.7 wt.% (Figs. 3 and 4b). Given the overlap of these values, the choice of method has a minimal effect on calculated decompression timescales, and we adopt the first approach here.

The external H₂O concentration was estimated specifically for each unit using the lowest H₂O value measured in the interiors of REs from that sample (Online Supplementary Table 4). These concentrations are similar to the lowest MI H₂O concentration measured in that same horizon (Fig. 4a). REs were used for this purpose because they rapidly re-equilibrate with the surrounding depressurized melt (within hours). Decompression timescales for each MI were modeled assuming an instantaneous pressure drop (step function), yielding the fastest decompression timescale and giving us the minimum possible ascent time. A more realistic scenario would be that each MI responded to a constantly decreasing external H₂O concentration throughout its ascent until it reached the depth at which the interiors of REs last equilibrated. This method, however, would yield longer timescales and requires a greater number of model assumptions that are not easily constrained, so we have adopted the first, simpler approach.

Minimum timescales for H₂O loss from each MI (using inclusion size and distance from crystal rim as input conditions) were calculated using the diffusion model of Cottrell et al. (2002). This model assumes a spherical MI in the center of a spherical phenocryst. In our model calculations, we chose the radius of the quartz phenocryst to be the minimum distance (rather than the average) between the actual MI and the crystal rim (measured in 2D section, Online Supplementary Table 1). Thus our model-derived times are again minima.

Most MIs (~78%, $n = 93$) yield decompression times from <12 h to 5 days, whereas the lowest measured H₂O concentrations (~1 wt.%) imply as long as two weeks (Fig. 4a; Supplementary Fig. 4b). This variability reveals that HRT magma ascent was complex: single fall layers contain crystals from both faster ascending magma (<12 h) and magma that had decompressed to varying degrees for varying times within the conduit system (days to weeks). The MI evidence for ascent times of hours to weeks for co-erupted crystals in single layers requires that magma rose and was released episodically over corresponding periods of days to weeks to generate the fall deposits studied (see Fig. 1, Supplementary Fig. 1). This interpretation finds qualitative support in the episodic deposition and periodic reworking of individual beds within the fall deposits.

To translate these diffusive loss times into ascent rates, an initial storage depth before diffusive loss began is required. An entrapment pressure for each MI can be calculated using the restored H₂O and measured CO₂ concentration (Fig. 4b). These pressures, which should represent the crystallization pressures of the quartz hosts, are converted into depths using a crustal density of 2600 kg/m³. For the inclusions that experienced <12 h of diffusive loss, ascent rates are >0.1 m/s, whereas inclusions that underwent days of diffusive loss ascended much more slowly, at apparent rates of ~0.01–0.005 m/s. These slow rates could be the result of either slow, continuous magma ascent, as occurs in dome forming eruptions (Melnik and Sparks, 1999), or more rapid ascent, with periodic stalling at shallower depths in the conduit (e.g. Cashman and McConnell, 2005; Riker et al., 2015).

It is possible that our estimated entrapment pressures overestimate the starting depth before ascent, because the CL zoning patterns of the quartz reveal a complex history for each crystal between the original time of trapping and final eruption (Supplementary Fig. 2). The minimum starting depth for melt containing these quartz crystals is constrained using the pressure at which H₂O solubility is ~4 wt.%, consistent with the highest concentrations found in inclusions from each sample (Fig. 4). Storage at lower pressure for a week or longer would cause reequilibration to lower values (Fig. 4, Supplementary Fig. 3). The 4 wt.% H₂O solubility value corresponds to depths closer to 4 km (1000 bars; Fig. 4), which would (at most) reduce our estimated ascent rates by a factor of two (Supplementary Table 4).

The variable range of ascent rates for co-erupted quartz in the HRT fall deposits has an intriguing parallel with the activity at Mount St. Helens from May 25 to October 1980. Eruptions during this period involved lava dome formation (from June to August) punctuated by explosive episodes (Rutherford and Hill, 1993; Blundy et al., 2010). Pumices from the explosive episodes contain amphiboles with breakdown-rim thicknesses that imply residence in magma for varying durations outside the amphibole stability field during ascent. Experimental data link the range in breakdown-rim thicknesses to timescales of up to 16 days (Rutherford and Hill, 1993), equivalent to ascent rates of 0.004–0.007 m/s for effusive magma, to >0.018 m/s for magma feeding the explosive episodes (i.e., no breakdown rims present). The diversity within single clasts was interpreted to result from mixing in the conduit of slowly ascending magma (feeding dome extrusion in the MSH case) with more rapidly ascending magma (feeding explosive activity). Subsequent work using

plagioclase and pumice textures reached similar conclusions for the summer 1980 explosive eruptions, whereby deeper, volatile-rich magma co-erupted with shallower degassed magma that had been stored within the conduit (Cashman and McConnell, 2005; Riker et al., 2015). Diverse H₂O contents of plagioclase-hosted MIs from the summer 1980 explosive eruptions (Blundy et al., 2010) could also be interpreted to reflect variable amounts of diffusive loss, reflecting slow ascent and mixing processes. These ascent models can be applied to explain our HRT dataset, where in any individual layer, co-erupted quartz crystals have experienced varied decompression histories.

5.4. Final ascent rates from modeling of volatile gradients in reentrants

Melt-filled reentrants (REs) are not sealed off by crystal growth and therefore record late-stage changes in the melt surrounding the host crystal. In contrast to MIs, which experience loss of H₂O but not CO₂, REs lose both H₂O and CO₂ by diffusion to the surrounding degassing melt during ascent. As decompression causes volatile exsolution from the host melt, it creates H₂O and CO₂ gradients in the REs that can be modeled to estimate ascent timescales (Liu et al., 2007; Humphreys et al., 2008; Lloyd et al., 2014). Importantly, the HRT REs show total H₂O (molecular + hydroxyl) values that decrease outwards towards the exterior melt with relatively constant OH⁻/H₂O_{molecular} ratios. Secondary hydration is thus inferred to be absent as it would result in increasing H₂O_{molecular} towards the mouth of the RE (Liu et al., 2007).

Concentration maps were measured by FTIR for 10 REs (100–280 μm in length), providing H₂O and CO₂ profiles with a spatial resolution of ~20 μm (Fig. 5a). Because CO₂ diffuses at a slower rate than H₂O, modeling both gradients simultaneously provides more robust constraints on ascent timescales. We compared our measured H₂O and CO₂ profiles to simulated profiles for various ascent rates calculated with a one dimensional diffusion code (modified from Liu et al., 2007), and constrained our dataset with those ascent rates that most closely reconstructed our measured profiles. REs with simple rectilinear geometries were favored for modeling. An overall homogeneity in the concentration maps for H₂O and CO₂ in the direction orthogonal to the main diffusional direction implies that a 1-D model does not introduce significant error to the calculated timescales (Fig. 5a).

For our model, the innermost concentrations were used as starting conditions because this assumption gave the best agreement between simulated and measured H₂O and CO₂ profiles. Using the average H₂O and CO₂ concentrations for MIs from a given sample as a starting condition or using a specific MI in the same crystal as the modeled RE both yielded poorer fits to the data. Lloyd et al. (2014) emphasized the importance of the RE having an observable bubble at its mouth in order to ensure accurate placement of the external boundary in the model calculations. The majority of our REs, however, lack such a bubble, but the glass in the REs is continuous with glass adhering to the quartz rim. We simulated profiles for which the external boundary of the RE was assumed to be coincident with the crystal rim, and another set of profiles for which the external boundary was extended 50 μm outward from the quartz rim (a realistic distance to the nearest bubble in an exsolving rhyolitic magma). Best-fit profiles were achieved using the rim as the boundary condition. To simulate changes in the external melt H₂O and CO₂ concentrations during decompression, which are time-dependent, we used models for open-system degassing and for closed-system degassing with 1 wt.% initial exsolved gas (Fig. 5b, c; Supplementary Fig. 6).

In the model calculations, diffusion is assumed to cease at the fragmentation depth, because the timescale between fragmentation and quenching of pyroclasts in the plume is likely to be very

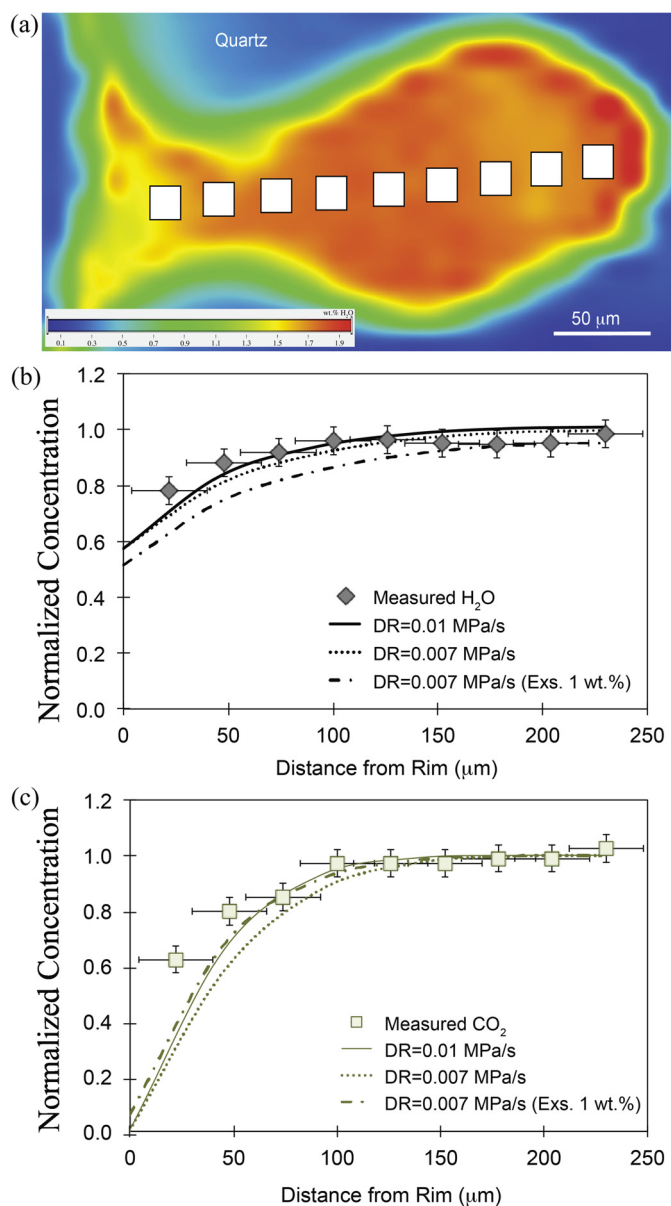


Fig. 5. (a) H_2O concentration map for a 200 μm -long reentrant from sample MM7 (blue = 0.1 wt.% H_2O ; red = 1.9 wt.%). The nine white boxes represent the FTIR aperture locations ($20 \times 20 \mu\text{m}$) used for measurement of H_2O (b) and CO_2 (c) concentration profiles. Concentration profiles for ten reentrants from six units were modeled using the diffusion code of Liu et al. (2007) to constrain decompression rates (panels b and c). The first two curves in each best-fit model (solid and dotted lines) are for open-system degassing, whereas the third curve (dashed line) represents a closed-system model with 1 wt.% exsolved gas (Liu et al., 2007). Additional assumptions and boundary conditions are discussed in the text and Supplementary material.

short (see discussion in Liu et al., 2007). Estimates of fragmentation pressure for hydrous rhyolitic magmas are mostly in the range of 10–30 MPa based on H_2O contents preserved in matrix glasses (Thomas et al., 1994) and critical bubble volume fraction (Sparks, 1978; Thomas et al., 1994). Following Liu et al. (2007), we chose a single value of 10 MPa. Based on calculations for REs with a range of sizes, the uncertainty associated with the choice of fragmentation pressure introduces a factor of 1.4–1.6 variability in ascent rates (Liu et al., 2007).

Decompression rates determined from the H_2O and CO_2 profiles (Fig. 5b, c; Supplementary Fig. 6) result in estimated ascent times of <1 to 4 h and ascent rates of ~ 0.3 –1.5 m/s. These rates

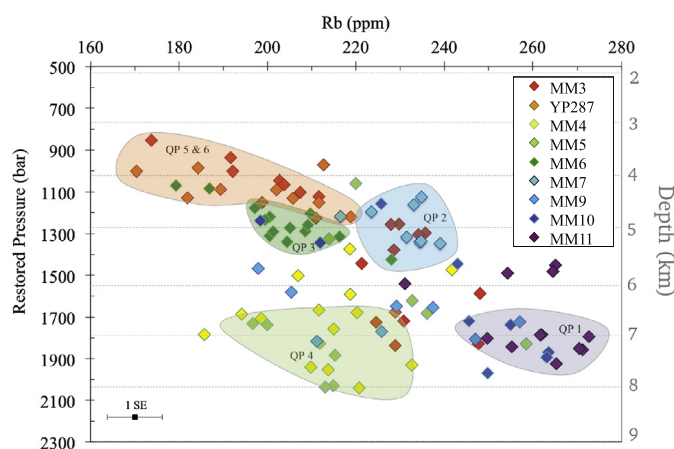


Fig. 6. Restored pressures (from Fig. 4) vs. Rb for all MIs. Pressures were converted to depths using a crustal density of 2600 kg/m^3 . The range in crystallization pressures is strongly controlled by the concentration of CO_2 in the MIs (Fig. 4). Colored fields delineate MI groups that correspond to five of the six quartz populations deduced from cluster analysis of MI compositions (see Section 6.1 for details). The color of each quartz population is based on the sample that contains the majority of that quartz population. For example, sample MM11 is represented completely by quartz population 1 and therefore is noted on the figures using the same color as MM11. Although quartz populations 5 and 6 have similar storage regions and Rb concentrations in this figure, they are distinguished on the basis of their Ba and Sr concentrations (see Fig. 7 and Supplementary Figs. 5, 6).

are similar to those of MIs that we infer to have experienced little to no H_2O loss (Fig. 4a, Supplementary Fig. 4b). This is consistent with our model of slowly ascending magma in the conduit being mixed with more rapidly ascending magma during punctuated, explosive eruptions. The final ascent rates for HRT magmas are notably slower than those inferred using the RE technique for moderate-sized explosive eruptions, for example, May 18, 1980 Mount St. Helens (Humphreys et al., 2008) and Fuego (Lloyd et al., 2014). The ascent rates are, however, similar to those for of the Oruanui supereruption (Liu et al., 2007), which also shows time breaks between units in its fall deposits (Wilson, 2001).

6. Trace-element evidence for sequential tapping of discrete magma bodies

Trace element concentrations in MIs ($n = 105$), REs ($n = 81$), and obsidian pyroclasts ($n = 23$) measured using LA-ICP-MS techniques provide further information on onset conditions for the HRT eruption.

6.1. Trace elements in melt inclusions

Concentrations of Ba, Rb, Sr, Cl, Nb and CO_2 (among other elements) cluster the MI data into distinct groups. For example, Rb values and restored entrapment pressures group the MIs into two main storage depths and five compositional populations (Fig. 6). Entrapment pressures indicate that although earlier erupted samples MM10 and MM11 have the most evolved compositions and H_2O -rich MIs (Figs. 3, 4) they crystallized at greater depths (6–8 km) than MIs in the least evolved, later erupted units (samples MM3 and YP287: 4–5 km; Fig. 6). In addition, another MI population in sample MM3 is revealed by Rb/Zr and Ba/Sr ratios that plot along a separate evolutionary trend (Supplementary Fig. 7). These relationships demonstrate that the MI compositions cannot reflect a single zoned magma chamber. We thus infer that the unique clusters, and separate trends, represent distinct crystallizing magma domains that evolved from chemically similar parent magma(s) but were spatially separated during crystallization.

To test the robustness of multiple MI groups based on trace element data (Fig. 6, Fig. 7a, Supplementary Fig. 7), we used the

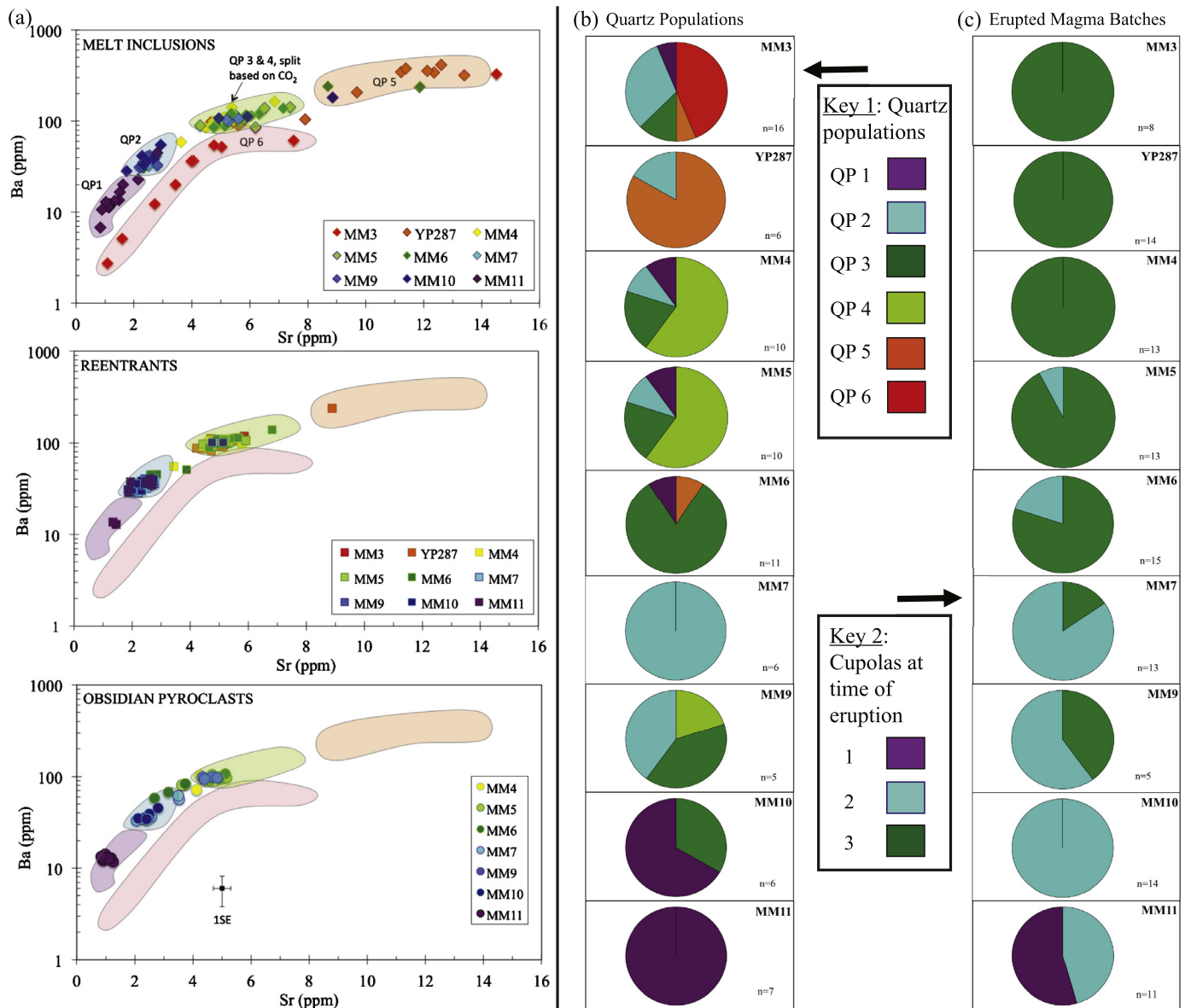


Fig. 7. (a) Concentrations of Sr vs. Ba for all melt inclusions (MIs: top panel, shown as diamonds), reentrants (REs: middle panel, shown as squares), and obsidian pyroclasts (bottom panel, shown as circles). The six quartz populations based on cluster analysis of MI compositions (as described in the text) are highlighted as colored fields in all panels. Reentrant and obsidian pyroclast compositions fall into three of the six quartz populations, suggesting that three distinct magma bodies were present at the time of eruption. Obsidian pyroclasts from MM3 and YP287 were not analyzed. (b) Distribution of quartz populations based on cluster analysis of MI compositions (see Section 6.1 for details). Each of the nine stratigraphic layers studied is shown by an individual pie diagram. The proportions of quartz in each sample that come from the six quartz populations (Key 1) are shown by colors within each pie. (c) Distribution of compositions for REs and obsidian pyroclasts, both of which represent the host melts at the time of eruption (Key 2). The RE and obsidian compositions fall into the fields for three of the six quartz populations (see middle and lower panels in a). Each pie diagram shows the proportion of the three compositional types of REs and obsidians in a particular sampled layer. Colors for the three populations were chosen to match the colors for the quartz population whose MIs are compositionally similar to the REs and obsidians (see middle and lower panels in a). The limited overlap between the three clusters of RE and obsidian composition suggests that there were three compositionally distinct magma bodies or batches that were vented over the portion of the HRT eruption represented by our sampling (see text for discussion).

statistical program JMP® (Version 10: SAS Institute Inc., Cary, North Carolina, 1989–2007). Variables that most clearly distinguished compositional groups (CaO, Cl, CO₂, Sr, B, Nb, Eu, Ba, Ta, and Rb) were selected for a multi-component cluster analysis. The results indicated six clusters based on MI composition. After identifying the clusters, we used discriminant function analysis to assess the significance of the results. This showed that there is only a 4% probability that a given MI would be assigned to the wrong cluster based on the ten variables that were used. We thus interpret the six clusters of MI composition to indicate six distinct populations of host quartz crystals (Fig. 7b). This evidence for six distinct quartz populations (revealed by MI compositions) suggests that the quartz crystals in fall deposits from the onset of the HRT eruption

originally formed in six chemically distinct crystallizing magma bodies.

Of the nine horizons sampled (Fig. 1b), some contain a mixture of the six quartz populations (samples MM3, MM4, MM5, MM9), whereas others contain crystals from primarily one population (samples YP287, MM6, MM7, MM10, MM11; see Fig. 7b). Of particular relevance is the relationship between quartz populations and stratigraphic position. Although later erupted units contain quartz crystals with similar MI compositions to the first eruptive units (e.g. quartz population 1 appears sporadically in MM3–6), there is no evidence for the opposite (e.g. quartz populations 5 or 6 do not occur at levels below sample MM6; see Fig. 7b).

Table 1
Average major (EPMA; in wt.%, Cl, F in ppm) and trace element (LA-ICP-MS in ppm) compositions, with variability given as 1 SD (italics), for the six quartz populations determined using melt inclusions (see Section 5 for discussion, Fig. 7), and the final three erupted cupolas based upon reentrant and obsidian pyroclast compositions (see Section 6 for discussion, Fig. 7, Supplementary Fig. 8). Major element, Cl and F values are normalized to 100% on an H₂O-free basis.

| | Quartz population 1 | Quartz population 2 | Quartz population 3 | Quartz population 4 | Quartz population 5 | Quartz population 6 | Eruptive cupola 1 | Eruptive cupola 2 | Eruptive cupola 3 |
|--------------------------------|---------------------|---------------------|---------------------|---------------------|---------------------|---------------------|-------------------|-------------------|-------------------|
| SiO ₂ | 76.23 0.60 | 76.28 0.36 | 76.66 0.42 | 76.28 0.38 | 76.15 0.30 | 76.56 0.18 | 76.86 0.39 | 76.80 0.48 | 76.65 0.54 |
| TiO ₂ | 0.08 0.01 | 0.09 0.02 | 0.09 0.01 | 0.11 0.02 | 0.12 0.01 | 0.10 0.01 | 0.08 0.01 | 0.08 0.02 | 0.10 0.02 |
| Al ₂ O ₃ | 12.39 0.41 | 12.11 0.28 | 12.05 0.29 | 12.26 0.30 | 12.15 0.23 | 12.27 0.25 | 12.27 0.27 | 12.13 0.30 | 12.10 0.44 |
| FeO | 1.28 0.11 | 1.40 0.10 | 1.41 0.08 | 1.46 0.06 | 1.53 0.09 | 1.41 0.06 | 1.21 0.11 | 1.38 0.13 | 1.43 0.13 |
| MgO | 0.01 0.00 | 0.02 0.00 | 0.02 0.00 | 0.02 0.00 | 0.03 0.00 | 0.02 0.00 | 0.01 0.00 | 0.02 0.00 | 0.02 0.00 |
| CaO | 0.55 0.03 | 0.55 0.01 | 0.55 0.02 | 0.57 0.01 | 0.47 0.09 | 0.44 0.04 | 0.55 0.02 | 0.54 0.02 | 0.55 0.02 |
| Na ₂ O | 3.98 0.19 | 3.68 0.41 | 3.59 0.26 | 3.73 0.17 | 4.12 0.31 | 3.99 0.06 | 4.05 0.13 | 3.66 0.43 | 3.55 0.34 |
| K ₂ O | 5.07 0.23 | 5.46 0.47 | 5.34 0.27 | 5.19 0.21 | 5.06 0.15 | 4.90 0.08 | 4.97 0.14 | 5.29 0.23 | 5.45 0.34 |
| Cl | 1889 86 | 1688 108 | 1560 99 | 1527 61 | 1272 36 | 1434 74 | 1830 129 | 1687 112 | 1478 101 |
| F | 2698 345 | 2338 443 | 2188 206 | 2177 448 | 2557 1185 | 1579 461 | 3301 1499 | 3473 1348 | 3085 1090 |
| Li | 78.8 7.8 | 56.0 22.4 | 46.8 23.5 | 55.9 10.5 | 70.0 20.8 | 81.1 23.7 | 61.7 9.7 | 47.9 11.8 | 42.6 14.8 |
| B | 17.5 3.3 | 13.4 1.4 | 12.5 1.1 | 12.9 1.4 | 11.1 1.6 | 12.7 0.8 | 16.5 1.9 | 15.2 1.8 | 12.9 1.7 |
| P | 54.8 10.5 | 54.4 9.0 | 60.9 8.5 | 58.8 11.1 | 75.3 8.1 | 54.3 7.3 | 58.2 4.1 | 60.1 8.3 | 63.4 12.9 |
| Ti | 52.0 5.5 | 61.4 6.7 | 67.5 2.9 | 69.5 3.2 | 82.3 6.4 | 69.6 3.7 | 47.9 2.2 | 55.2 2.8 | 65.8 3.2 |
| Rb | 259 12 | 230 8 | 208 14 | 211 10 | 191 14 | 212 16 | 263 9 | 242 11 | 220 12 |
| Sr | 1.7 0.6 | 3.5 1.4 | 5.6 0.6 | 5.7 0.9 | 11.9 1.6 | 5.0 1.3 | 1.1 0.2 | 2.4 0.2 | 5.0 0.4 |
| Y | 82.1 14.0 | 82.9 5.2 | 78.6 9.0 | 75.3 4.2 | 66.8 3.6 | 74.6 6.1 | 80.6 4.9 | 82.4 6.2 | 74.0 5.9 |
| Zr | 173 39.5 | 204 10.2 | 211 27.4 | 210 13.5 | 227 37.0 | 206 14.9 | 148 10.4 | 200 13.4 | 199 15.4 |
| Nb | 71.8 6.7 | 70.0 2.5 | 63.7 4.0 | 64.1 3.6 | 56.9 4.6 | 65.6 3.6 | 71.0 2.7 | 69.5 2.9 | 62.7 3.0 |
| Sn | 6.9 0.5 | 6.0 0.5 | 5.4 0.4 | 5.4 0.4 | 4.8 0.5 | 5.6 0.3 | 7.2 0.4 | 6.6 0.6 | 5.7 0.5 |
| Ba | 20.9 12.1 | 56.4 33.5 | 107 13.2 | 112.6 24.0 | 318 80.7 | 60.0 29.0 | 12.7 1.0 | 36.2 3.9 | 101 6.9 |
| La | 45.7 16.7 | 65.6 8.8 | 72.0 8.2 | 71.8 5.2 | 86.6 12.3 | 71.3 5.6 | 33.0 1.4 | 62.1 3.8 | 66.7 5.2 |
| Ce | 101 27.8 | 134 12.8 | 142 8.7 | 145 7.0 | 172 20.0 | 144 9.2 | 79.0 2.9 | 132 6.0 | 137 5.1 |
| Pr | 10.4 3.0 | 13.8 1.4 | 14.6 1.4 | 14.6 0.8 | 16.7 2.1 | 14.5 1.0 | 8.4 0.4 | 13.5 0.9 | 13.8 0.8 |
| Nd | 40.9 11.8 | 53.7 5.2 | 56.5 5.3 | 56.2 3.6 | 64.7 9.2 | 56.3 5.0 | 33.4 1.6 | 52.7 4.0 | 53.1 3.5 |
| Sm | 10.4 2.2 | 12.4 1.5 | 12.4 1.9 | 12.1 1.0 | 12.6 1.9 | 12.0 1.3 | 9.2 0.9 | 12.3 1.2 | 11.9 1.1 |
| Eu | 0.2 0.1 | 0.3 0.1 | 0.4 0.1 | 0.4 0.1 | 0.8 0.2 | 0.4 0.1 | 0.2 0.0 | 0.3 0.0 | 0.4 0.1 |
| Gd | 11.8 2.0 | 13.4 1.2 | 13.1 1.7 | 12.8 1.2 | 12.3 1.7 | 12.6 1.3 | 11.1 0.5 | 13.3 1.5 | 12.4 1.0 |
| Dy | 14.1 2.5 | 14.5 0.9 | 13.8 1.5 | 13.5 1.2 | 12.3 0.9 | 13.3 1.1 | 13.9 1.3 | 14.6 1.3 | 13.0 1.2 |
| Er | 9.1 1.9 | 9.3 0.8 | 8.8 1.0 | 8.5 0.3 | 7.1 0.6 | 8.4 0.5 | 9.0 1.0 | 9.3 0.8 | 8.3 0.8 |
| Yb | 8.2 1.1 | 7.9 0.8 | 7.6 0.8 | 7.5 0.5 | 6.5 0.4 | 7.3 0.5 | 8.0 0.7 | 8.1 0.7 | 7.2 0.7 |
| Hf | 7.8 1.7 | 8.6 0.9 | 8.6 1.0 | 8.4 0.8 | 8.4 1.1 | 8.5 0.9 | 6.9 0.6 | 8.5 0.9 | 8.2 0.9 |
| Ta | 4.7 0.8 | 4.7 0.3 | 4.1 0.3 | 4.2 0.3 | 3.5 0.2 | 4.2 0.3 | 4.7 0.4 | 4.6 0.3 | 4.0 0.3 |
| Pb | 45.6 3.4 | 39.9 3.7 | 37.8 4.1 | 37.6 2.2 | 32.0 2.6 | 34.6 2.5 | 45.1 3.4 | 43.1 2.7 | 38.3 2.6 |
| Th | 28.1 5.6 | 30.0 2.1 | 29.3 2.3 | 28.9 1.9 | 28.6 1.3 | 28.6 2.3 | 26.3 1.6 | 30.2 1.9 | 27.1 2.0 |
| U | 9.0 0.6 | 8.1 0.6 | 7.4 0.5 | 7.7 0.5 | 6.6 0.4 | 7.5 0.5 | 9.3 0.5 | 8.8 0.7 | 7.4 0.4 |

6.2. Trace elements in reentrants and obsidian pyroclasts

Here we evaluate the extent to which the six distinct magma bodies in which the quartz populations originally crystallized were still present at the time of eruption, using the compositions of REs and obsidian pyroclasts as a record of the host melts surrounding the quartz crystals on evacuation. The geochemical similarity of the obsidian pyroclasts to the RE populations in each fall deposit layer (Fig. 7a; and Supplementary Fig. 8) suggests that both pyroclasts and REs represent external, host melt compositions at the time of eruption. Of the ~81 REs analyzed, >90% fall into two distinct populations, one of which overlaps with quartz population 2, and the other appears to be a mixture of quartz populations 3 and 4 (Fig. 7a; Supplementary Fig. 8). This observation implies that much of the compositional diversity associated with the quartz populations was reduced between the time of MI entrapment and eruption, such that only two distinct magma bodies were present just before eruption. However, the obsidian pyroclasts from samples MM4–MM11 establish that a third melt, similar to quartz population 1, was also present as a distinct magma composition at the time of eruption (Fig. 7a). Together, the RE and obsidian pyroclast compositions establish that the six quartz populations based on MI compositions had been integrated into three distinct melt groups prior to eruption (Fig. 7; Supplementary Figs. 8 and 9). Average (± 1 s.d.) major and trace element compositions for melts in each of the six quartz populations and for the three melt groups present at the time of eruption are in Table 1.

We infer that these three melt groups represent three cupolas: chemically discrete, volumetrically minor bodies along the roof of the main magma volume that subsequently erupted to form the later ignimbrite members. However, whether the main magma volume was a unitary magma chamber or a distributed set of reservoirs of variable size (e.g., Fig. 15 in Cashman and Giordano, 2014) is currently under investigation (E.J.S. et al., unpublished data). As with the quartz populations (Fig. 7b), the proportion of material erupted from the three cupolas varies systematically with stratigraphy in the fall deposit, as follows (see Fig. 7c):

- Cupola 1 is represented in the first fraction of material erupted and is the most evolved and smallest in volume (dominant only in sample MM11), which was then followed by a reworking time break (Fig. 1). Material from Cupola 1 does not recur above the level of sample MM11 (Fig. 7c).
- Cupola 2 is represented in much of the material (samples MM9 and MM10) that makes up the sections between the reworked layers (Fig. 7c). Cupola 2 continued to be tapped up to the level sampled as MM5, but thereafter was absent. The presence of material from both cupolas 2 and 3 in samples MM9 through MM5 is inferred to represent co-deposition from two separate vents, with cupola 3 becoming dominant by the stage represented as sample MM6.
- Cupola 3 is represented in sample MM6 and above and was thus likely the largest in volume (Figs. 1 and 7; Supplementary Figs. 8 and 9). The vent for this cupola may have developed into a major structure as no time breaks, apart from those

represented by deposition of normally graded fall layers, are inferred to have occurred before ignimbrite deposition commenced at the Mount Everts location.

7. Implications for the onset of the Huckleberry Ridge eruption

Our dataset highlights the complexity and fine-scale detail that can be associated with the initiation of a large supereruption. Six compositionally distinct magma bodies (based on quartz-hosted MI compositions) had amalgamated into three cupolas (based on RE and obsidian pyroclast compositions) by the time of eruption (Fig. 7, Supplementary Figs. 8 and 9). Melt inclusions in each stratigraphic layer sampled experienced highly variable extents of H₂O diffusive loss, requiring prolonged ascent conditions from all eruptive vents (Supplementary Fig. 4b). The coherency of the RE and obsidian pyroclast glass compositions with stratigraphic position and the lack of geochemical evidence in pumice shards that the different compositions mixed or mingled within the conduit (E.J.S., unpublished data) necessitates that the cupolas were erupted sequentially from separate vents, but with some degree of temporal overlap (Fig. 7c, Supplementary Fig. 9). The nature of the compositional variations and their systematic stratigraphic ordering preclude them as resulting from the chaotic mixing or tapping of a single chemically stratified, physically integrated magma body. Our results, along with the field evidence, show that the initial Huckleberry Ridge eruptive activity was episodic and prolonged, with magma slowly ascending to feed periodic explosive activity, and with time breaks manifested by contemporaneous reworking in the fall deposits.

A key question then arises: what would allow an eruption (especially one of such magnitude) to stop once started, repetitively, with similarly prolonged ascent behavior at three separate vents? The prolonged decompression with punctuated explosive events could potentially be explained by the progressive development of a fracture network that becomes increasingly connected over time to form a transport system feeding magma to the surface, as has been proposed for the 1980 Mount St. Helens and 1991 Pinatubo eruptions (Scandone et al., 2007). However, our evidence for sequential eruption of three distinct magma bodies from separate vents, along with the episodic shutting off of the plume, suggests an external control for the initiation of the Huckleberry Ridge eruption. Furthermore, the slow ascent rates inferred from the variable H₂O losses from melt inclusions require low degrees of overpressure in the feeding magma bodies (Melnik and Sparks, 1999), consistent with the start/stop nature of the initial eruptive activity. It is important to note, though, that our data pertain only to the very initial eruption dynamics, and other factors may have become important in controlling the subsequent voluminous, caldera collapse-related parts of the eruption.

Parallels can be drawn with the 25.4 ka Oruanui eruption (Liu et al., 2007; Allan et al., 2012). The Oruanui fall deposits contain evidence for multiple eruption hiatuses (Wilson, 2001), and syn-eruptive lateral transport of a foreign magma type, which collectively are used to infer that the eruption was modulated in its early stages by tectonic mechanisms (Allan et al., 2012). Considering that several large regional faults intersect the HRT caldera area (Christiansen, 2001; Simakin and Ghassemi, 2010), we suggest that tectonic processes were the controlling factor on (and at) eruption onset. Movement along a fault-bound or dike-controlled structure would have permitted magma to ascend slowly from spatially separated locations, with intermittent eruptions controlled by changes in the stress regime (Fig. 8; Allan et al., 2012). The causes and effects between regional tectonic forces and those imposed by the presence of the magma body itself in causing any fault fracturing (Bursik et al., 2003; Hampel and Hetzel, 2008; Gregg et al., 2012) cannot, however, be resolved from our data.

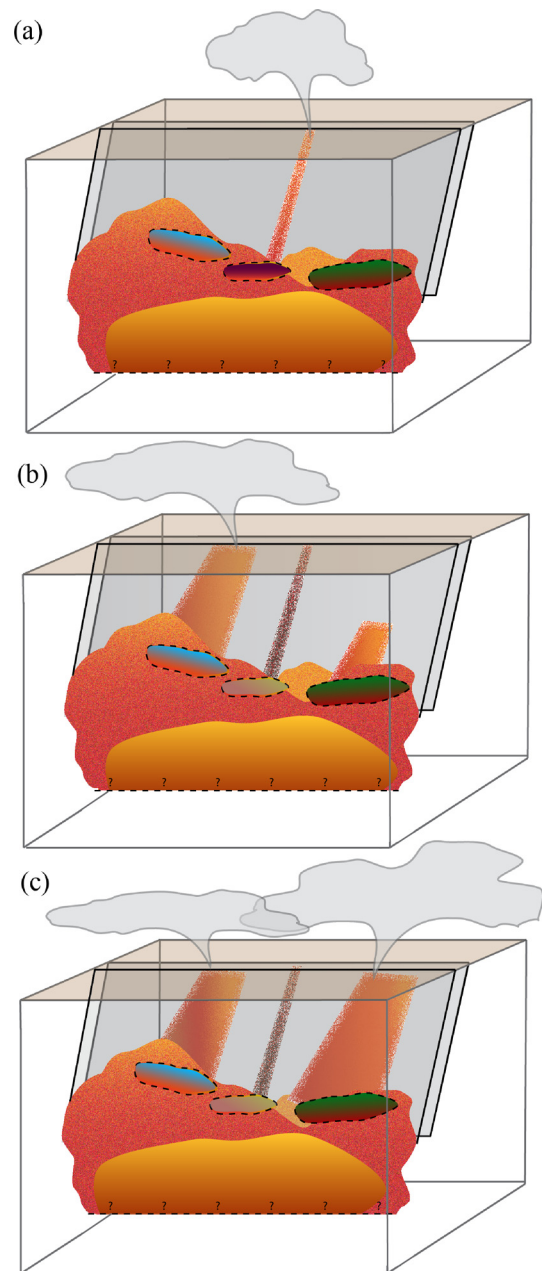


Fig. 8. Schematic interpretation for the earliest stages of the Huckleberry Ridge eruption, with three compositionally distinct magma cupolas (colors correspond to individual cupolas, see Key 2 in Fig. 7c) located above a larger magma body. Each cupola was tapped sequentially (see Section 6.2) in response to destabilization, likely due to tectonic processes. See Section 7 for more details.

Despite this uncertainty, our combined field and geochemical approach provides some of the first time-resolved evidence for prolonged decompression at the onset of a major caldera-forming eruption, and suggests that external factors may have modulated the initial eruptive behavior.

8. Conclusions

Insights into the mechanisms and timescales associated with the initiation of caldera-forming eruptions can be revealed using geochemical data for the earliest deposits that formed during eruption onset. Here we present geochemical data for the 2.5 m initial fall deposit of the Huckleberry Ridge eruption, which preserves evidence for multiple reworked layers that reflect short eruptive

pauses (each on the order of days) prior to the emplacement of voluminous ignimbrite. Our results reveal evidence for three distinct magma bodies that were erupted episodically and sequentially during eruption onset, most likely from separate vents. In addition, highly variable extents of H₂O diffusive losses from melt inclusions through quartz phenocrysts provide evidence for prolonged ascent times, suggesting that the magma bodies were not strongly over-pressured at eruption onset. Our evidence for sequential eruption of three distinct magma bodies, together with the start–stop nature of the eruption inferred from the deposits and comparisons with the Oruanui supereruption, suggest an external (likely tectonic) control modulated the initiation of the Huckleberry Ridge eruption. Our results reveal the complexity that can be resolved for the initiation of a large eruption, and raises the question as to whether similar evidence is present in other cases but has not been looked for. Furthermore, our work highlights a new geochemical approach for obtaining information about the immediate pre-eruptive state of magma bodies that could be applied to other systems to shed light on eruption triggering mechanisms.

Acknowledgements

Myers acknowledges the support of a USGS Kleinman Volcanology Grant for sample collection in Fall 2013. Wilson thanks Christy Hendrix and Stacey Gunther in the Yellowstone Research Office for permission (YELL-05248) to work in Yellowstone National Park, and the Royal Society of New Zealand for a James Cook Fellowship and previous support, under Marsden Fund grant VUW0813. Additional financial support was provided by National Science Foundation grant EAR-1524824 to Wallace. Swallow acknowledges receipt of a Commonwealth Scholarship administered by Universities New Zealand – Te Pūkai Tara. We are indebted to Jake Lowenstern, Yang Liu, and Leif Karlstrom for thoughtful discussions, and to Shan de Silva and an anonymous reviewer for constructive comments that greatly helped to clarify our presentation.

Appendix A. Supplementary material

Supplementary material related to this article can be found online at <http://dx.doi.org/10.1016/j.epsl.2016.07.023>.

References

- Allan, A.S.R., Wilson, C.J.N., Millet, M.-A., Wysoczanski, R.J., 2012. The invisible hand: tectonic triggering of a rhyolitic supereruption. *Geology* 40, 563–566.
- Almeev, R.R., Bolte, T., Nash, B.P., Holtz, F., Erdmann, M., Cathey, H.E., 2012. High-temperature, low-H₂O silicic magmas of the Yellowstone hotspot: an experimental study of rhyolite from the Bruneau–Jarbridge eruptive center, Central Snake River Plain, USA. *J. Petrol.* 53, 1837–1866.
- Barker, S.J., Wilson, C.J.N., Smith, E.G.C., Charlier, B.L.A., Wooden, J.L., Hiess, J., Ireland, T.R., 2014. Post-supereruption magmatic reconstruction of Taupo volcano (New Zealand), as reflected in zircon ages and trace elements. *J. Petrol.* 55, 1511–1533.
- Behrens, H., Tamic, N., Holtz, F., 2004. Determination of the molar absorption coefficient for the infrared absorption band of CO₂ in rhyolitic glasses. *Am. Mineral.* 89, 301–306.
- Blundy, J., Cashman, K.V., Rust, A., Witham, F., 2010. A case for CO₂-rich arc magmas. *Earth Planet. Sci. Lett.* 290, 289–301.
- Boehnke, P., Watson, E.B., Trail, D., Harrison, T.M., Schmitt, A.K., 2013. Zircon saturation re-revisited. *Chem. Geol.* 351, 324–334.
- Bursik, M., Renshaw, C., McCalpin, J., Berry, M., 2003. A volcanotectonic cascade: activation of range front faulting and eruptions by dike intrusion, Mono Basin–Long Valley Caldera, California. *J. Geophys. Res.* 108, 2393.
- Caricchi, L., Annen, C., Blundy, J., Simpson, G., Pinel, V., 2014. Frequency and magnitude of volcanic eruptions controlled by magma injection and buoyancy. *Nat. Geosci.* 7, 126–130.
- Cashman, K.V., Giordano, G., 2014. Calderas and magma reservoirs. *J. Volcanol. Geotherm. Res.* 288, 28–45.
- Cashman, K.V., McConnell, S.M., 2005. Multiple levels of magma storage during the 1980 summer eruptions of Mount St. Helens, WA. *Bull. Volcanol.* 68, 57–75.
- Charlier, B.L.A., Morgan, D.J., Wilson, C.J.N., Wooden, J.L., Allan, A.S.R., Baker, J.A., 2012. Lithium concentration gradients in feldspar and quartz record the final minutes of magma ascent in an explosive supereruption. *Earth Planet. Sci. Lett.* 319, 218–227.
- Christiansen, R.L., 2001. The Quaternary and Pliocene Yellowstone Plateau volcanic field of Wyoming, Idaho, and Montana. *U. S. Geol. Surv. Prof. Pap.* 729-G, G1–G143.
- Cottrell, E., Spiegelman, M., Langmuir, C.H., 2002. Consequences of diffusive re-equilibration for the interpretation of melt inclusions. *Geochem. Geophys. Geosyst.* 3, 1026.
- de Silva, S.L., Gregg, P.M., 2014. Thermomechanical feedbacks in magmatic systems: implications for growth, longevity, and evolution of large caldera-forming magma reservoirs and their supereruptions. *J. Volcanol. Geotherm. Res.* 282, 77–91.
- Dixon, J.E., Stolper, E.M., Holloway, J.R., 1995. An experimental study of water and carbon dioxide solubilities in mid-ocean ridge basaltic liquids. Part I: calibration and solubility models. *J. Petrol.* 36, 1607–1631.
- Donovan, J.J., Kremser, D., Fournelle, J.H., 2007. Probe for Windows User's Guide and Reference, Enterprise edition. Probe Software, Inc., Eugene, OR.
- Ghiorso, M.S., Gualda, G.A.R., 2015. An H₂O–CO₂ mixed fluid saturation model compatible with rhyolite-MELTS. *Contrib. Mineral. Petrol.* 169, 1–30.
- Gregg, P.M., de Silva, S.L., Grosfils, E.B., Parmigiani, J.P., 2012. Catastrophic caldera-forming eruptions: thermomechanics and implications for eruption triggering and maximum caldera dimensions on Earth. *J. Volcanol. Geotherm. Res.* 241–242, 1–12.
- Gregg, P.M., Grosfils, E.B., de Silva, S.L., 2015. Catastrophic caldera-forming eruptions II: the subordinate role of magma buoyancy as an eruption trigger. *J. Volcanol. Geotherm. Res.* 305, 100–113.
- Hampel, A., Hetzel, R., 2008. Slip reversals on active normal faults related to the inflation and deflation of magma chambers: numerical modeling with application to the Yellowstone–Teton region. *Geophys. Res. Lett.* 35, L07301.
- Humphreys, M., Menand, T., Blundy, J.D., Klimm, K., 2008. Magma ascent rates in explosive eruptions: constraints from H₂O diffusion in melt inclusions. *Earth Planet. Sci. Lett.* 270, 25–40.
- Jellinek, A.M., DePaolo, D.J., 2003. A model for the origin of silicic magma chambers: precursors of caldera-forming eruptions. *Bull. Volcanol.* 65, 363–381.
- Johnson, E.A., Rossman, G.R., 2013. The diffusion behavior of hydrogen in plagioclase feldspar at 800–1000 °C: implications for re-equilibration of hydroxyl in volcanic phenocrysts. *Am. Mineral.* 98, 1779–1787.
- Leschik, M., Heide, G., Frischat, G.H., Behrens, H., Wiedenbeck, M., Wagner, N., Heide, K., Geißler, H., Reinholz, U., 2004. Determination of H₂O and D₂O contents in rhyolitic glasses. *Phys. Chem. Glasses, Eur. J. Glass Sci. Technol. B* 45, 238–251.
- Liu, Y., Anderson, A.T., Wilson, C.J.N., 2007. Melt pockets in phenocrysts and decompression rates of silicic magmas before fragmentation. *J. Geophys. Res.* 112, B06204.
- Lloyd, A.S., Plank, T., Ruprecht, P., Hauri, E.H., Rose, W., 2013. Volatile loss from melt inclusions in pyroclasts of differing sizes. *Contrib. Mineral. Petrol.* 165, 129–153.
- Lloyd, A.S., Ruprecht, P., Hauri, E.H., Rose, W., Gonnermann, H.M., Plank, T., 2014. NanoSIMS results from olivine-hosted melt embayments: magma ascent rate during explosive basaltic eruptions. *J. Volcanol. Geotherm. Res.* 283, 1–18.
- Loewen, M.W., Bindeman, I.N., 2015. Oxygen isotope and trace element evidence for three stage petrogenesis of the youngest episode (260–79 ka) of Yellowstone rhyolitic volcanism. *Contrib. Mineral. Petrol.* 170, 1–25.
- Malfait, W.J., Seifert, R., Petitgirard, S., Perrillat, J.P., Mezouar, M., Ota, T., Nakamura, E., Lerch, P., Sanchez-Valle, C., 2014. Supervolcano eruptions driven by melt buoyancy in large silicic magma chambers. *Nat. Geosci.* 7, 122–125.
- Mason, B.G., Pyle, D.M., Oppenheimer, C., 2004. The size and frequency of the largest explosive eruptions on Earth. *Bull. Volcanol.* 66, 735–748.
- Melnik, O., Sparks, R.S.J., 1999. Nonlinear dynamics of lava dome extrusion. *Nature* 402, 37–41.
- Newman, S., Lowenstern, J.B., 2002. VolatileCalc: a silicate melt–H₂O–CO₂ solution model written in Visual Basic for Excel. *Comput. Geosci.* 28, 597–604.
- Peppard, B.T., Steele, I.M., Davis, A.M., Wallace, P.J., Anderson, A.T., 2001. Zoned quartz phenocrysts from the rhyolitic Bishop Tuff. *Am. Mineral.* 86, 1034–1052.
- Qin, Z., 1992. Disequilibrium partial melting model and its implications for trace element fractionations during mantle melting. *Earth Planet. Sci. Lett.* 112, 75–90.
- Riker, J.M., Cashman, K.V., Rust, A.C., Blundy, J.D., 2015. Experimental constraints on plagioclase crystallization during H₂O- and H₂O–CO₂-saturated magma decompression. *J. Petrol.* 56, 1967–1998.
- Roberge, J., Wallace, P.J., Kent, A.J.R., 2013. Magmatic processes in the Bishop Tuff rhyolitic magma based on trace elements in melt inclusions and pumice matrix glass. *Contrib. Mineral. Petrol.* 165, 237–257.
- Roche, O., Druitt, T.H., 2001. Onset of caldera collapse during ignimbrite eruptions. *Earth Planet. Sci. Lett.* 191, 191–202.
- Rutherford, M.J., Hill, P.M., 1993. Magma ascent rates from amphibole breakdown: an experimental study applied to the 1980–1986 Mount St. Helens eruptions. *J. Geophys. Res.* 98, 19667–19685.
- Scandone, R., Cashman, K.V., Malone, S.D., 2007. Magma supply, magma ascent and the style of volcanic eruptions. *Earth Planet. Sci. Lett.* 253, 513–529.
- Self, S., 2006. The effects and consequences of very large explosive volcanic eruptions.

- tions. *Philos. Trans. R. Soc. Lond. A* 364, 2073–2097.
- Severs, M.J., Azbej, T., Thomas, J.B., Mandeville, C.W., Bodnar, R.J., 2007. Experimental determination of H₂O loss from melt inclusions during laboratory heating: evidence from Raman spectroscopy. *Chem. Geol.* 237, 358–371.
- Simakin, A.G., Ghassemi, A., 2010. The role of magma chamber-fault interaction in caldera forming eruptions. *Bull. Volcanol.* 72, 85–101.
- Skirius, C.M., 1990. Pre-eruptive H₂O and CO₂ content of Plinian and ash-flow Bishop Tuff magma. Ph.D. Dissertation. University of Chicago.
- Sparks, R.S.J., 1978. The dynamics of bubble formation and growth in magmas: a review and analysis. *J. Volcanol. Geotherm. Res.* 3, 1–37.
- Thomas, N., Jaupart, C., Vergnolle, S., 1994. On the vesicularity of pumice. *J. Geophys. Res.* 99, 15633–15644.
- Waters, L.E., Lange, R.A., 2015. An updated calibration of the plagioclase-liquid hygrometer-thermometer applicable to basalts through rhyolites. *Mineral.* 100, 2172–2184.
- Watson, E.B., Harrison, T.M., 1983. Zircon saturation revisited: temperature and composition effects in a variety of crustal magma types. *Earth Planet. Sci. Lett.* 64, 295–304.
- Wilson, C.J.N., 2001. The 26.5 ka Oruanui eruption, New Zealand: an introduction and overview. *J. Volcanol. Geotherm. Res.* 112, 133–174.
- Wilson, C.J.N., Hildreth, W., 1997. The Bishop Tuff: new insights from eruptive stratigraphy. *J. Geol.* 105, 407–439.
- Wysoczanski, R., Tani, K., 2006. Spectroscopic FTIR imaging of water species in silicic volcanic glasses and melt inclusions: an example from the Izu-Bonin arc. *J. Volcanol. Geotherm. Res.* 156, 302–314.
- Zhang, Y., Jenkins, J., Xu, Z., 1997. Kinetics of the reaction H₂O + O → 2OH in rhyolitic glasses upon cooling: geospeedometry and comparison with glass transition. *Geochim. Cosmochim. Acta* 61, 2167–2173.